Energy & Environmental Science

Accepted Manuscript

ROYAL SOCIETY OF CHEMISTRY

www.rsc.org/ees

Journal Name

ARTICLE

Received 00th January 20xx,

Accepted 00th January 20xx

DOI: 10.1039/x0xx00000x

www.rsc.org/

Porous P-doped graphitic carbon nitride nanosheets for synergistically enhanced visible-light photocatalytic H_2 production

Jingrun Ran,[a] Tian Yi Ma,[a] Guoping Gao,[b] Xi-Wen Du[c] and Shi Zhang Qiao*[a,c]

A novel porous P-doped graphitic carbon nitride nanosheets were for the first time fabricated by combining P doping and thermal exfoliation strategies. The as-prepared P-doped g-C_3N_4 nanosheets show the high visible-light photocatalytic H_2-production activity of 1596 μmol h^{-1} g^{-1} and apparent quantum efficiency of 3.56% at 420 nm, representing one of the most highly-active metal-free g-C_3N_4 nanosheets photocatalysts. This outstanding photocatalytic performance originates from the P-doped conjugated system and novel macroporous nanosheets morphology of PCN-S. Particularly, the empty midgap states (-0.16 V *vs.* Standard Hydrogen Electrode) created by P doping are for the first time found to greatly extend the light-responsive region up to 557 nm by density functional theory and experimental studies; whilst the novel macroporous structure promotes the mass-tranfser process and enhances light harvesting. Our study not only demonstrates a facile, eco-friendly and scalable strategy to syntheszie highly-efficient porous g-C_3N_4 nanosheets photocatalyst, but also paves a new avenue for the rational design and synthesis of advanced photocatalysts by harnessing the strong synergistic effects through simultaneously tuning and optimizing the electronic, crystallographic, surface and textural structures.

Introduction

Seeking highly efficient photocatalysts has been propelled by the prospect of converting sustainable solar energy into clean and carbon-free hydrogen fuel via photocatalytic water splitting.[1-8] Among numerous photocatalysts explored, graphitic carbon nitride (g-C_3N_4) has emerged as an attractive metal-free visible-light photocatalyst due to its advantageous features including abundance, nontoxicity, stability and chemical tenability.[9-13] However, the pristine g-C_3N_4 still suffers from unsatisfactory photocatalytic efficiency owing to its restricted visible-light harvesting capacity, ready recombination of charge carriers, and low surface area.[10-17] Thus, various modification approaches, such as elemental[10,14-30] and molecular doping,[31-33] exfoliation to two-dimensional (2D) nanosheets,[34-40] nanostructure design by templating,[41-43] supramolecular preorganization,[44-46] construction of g-C_3N_4 based heterojunctions[47,48] and dye sensitization,[49,50] are adopted to enhance its photocatalytic performance.

One important strategy to enhance the performance of g-C_3N_4 is to engineer its electronic structure by doping and hybridization with non-metal (*e.g.*, B, S, O, I)[10,14-26] or metal (*e.g.*, Fe, Zn, Cu) atoms.[27-30] This element doping strategy plays an essential role in tuning the band gap structure, extending the light absorption, increasing the charge transfer mobility and creating more active sites.[10,14-30] To date, only a few studies have concentrated on the P doped g-C_3N_4 for enhanced visible-light photocatalytic H_2 production.[20,26] For instance, Hu *et al.*[20] reported P-doped g-C_3N_4 exhibits 1.3 times higher photocatalytic H_2-production activity than undoped g-C_3N_4 when using $(NH_4)_2HPO_4$ as a precursor. Very recently, a novel copolymerization method using hexachlorocyclotriphosph-azene as the P precursor was also employed to prepare P-doped g-C_3N_4, which achieves a 2.9 times higher photocatalytic H_2-production rate than pristine g-C_3N_4.[26] However, the insightful understanding of the effect of P doping on the band gap structure and photocatalytic performance is still missing. Moreover, considering the important role of P precursors in influencing the photocatalytic performance,[26] the search for a new P precursor, which can obtain an even higher enhancement factor in photocatalytic performance, is highly desirable.

Very recently, 2D g-C_3N_4 nanosheets obtained from various exfoliation methods, such as liquid-exfoliation in organic solvents,[34-37] or acid media,[38] and thermal exfoliation,[39,40] have been extensively investigated in photocatalytic application because they can provide large surface area, abundant active sites, short charge diffusion distance and enhanced redox abilities of photo-generated electrons and holes.[34-40] However, one fatal problem associated with the 2D g-C_3N_4 nanosheets is its largely increased bandgap due to the strong quantum confinement effect (QCE) and decrease of conjugation length,

[a] School of Chemical Engineering, The University of Adelaide, Adelaide, SA 5005, Australia. E-mail: s.qiao@adelaide.edu.au
[b] School of Chemistry, Physics and Mechanical Engineering Faculty, Queensland University of Technology, Garden Point Campus, QLD 4001, Brisbane, Australia
[c] School of Materials Science and Engineering, Tianjin University, Tianjin, 300072, P. R. China
† Electronic Supplementary Information (ESI) available. See
DOI: 10.1039/x0xx00000x

which seriously limits its practical application for solar energy conversion. To solve this problem, two methodologies are available. While band gap engineering is necessary for extending the light-absorption region, the introduction of macroporous structure can enhance light harvesting by inner reflections.[51,52] However, to the best of our knowledge, the simultaneous band gap engineering and macropores creating on 2D g-C_3N_4 nanosheets for achieving synergistically enhanced photocatalytic H_2-production activity has not been reported yet.

Herein we for the first time report a simple, environmental-friendly and scalable method to synthesize novel porous P-doped g-C_3N_4 nanosheets (PCN-S) by a combination of P doping and thermal exfoliation. The as-synthesized PCN-S exhibits an outstanding visible-light photocatalytic H_2-production activity and robust reliability. To investigate the origin of such a high photocatalytic performance, both theoretical and experimental studies were performed.

Experimental section

Materials preparation

All the reagents were of analytical grade and were used without further purification. De-ionized water was used in all experiments. Bulk P-doped g-C_3N_4 (PCN-B) was synthesized by a P doping method. Since preliminary studies suggest that PCN-B with a mass ratio 2-aminoethylphosphonic acid (AEP): melamine (ME) of 1:60 showed the highest photocatalytic H_2-production activity (see Fig. S1, ESI†), this mass ratio was chosen in the current study. In detail, AEP and ME with a mass ratio of 1:60 were dissolved in de-ionized water and heated to 80 °C. Then the water was evaporated at 80 °C. The resulting complex crystal was ground to powder and heated in a covered quartz container from room temperature to 500 °C in N_2 flow, and kept at 500 °C for 3 hours. Then the temperature was increased to 550 °C and the sample was further heated for 5 hours. The resulting brown agglomerates were milled into powder in a mortar. Porous PCN-S were synthesized by thermal exfoliation of the above-obtained PCN-B in an open quartz container, which was heated from room temperature to 500 °C in static air, and kept at 500 °C for 2 hours. The resulting light-brown agglomerates were milled into powder in a mortar. Bulk P-doped g-C_3N_4* (PCN-B*) was synthesized by using $(NH_4)_2HPO_4$ as the P precursor according to the study by Hu *et al*.[20] Bulk g-C_3N_4 (CN-B) was synthesized by the same method for preparing PCN-B except that only ME was subjected to thermal poly-condensation. The resulting yellow agglomerates were milled into powder in a mortar. g-C_3N_4 nanosheets (CN-S) were synthesized by thermal exfoliation of the above-prepared CN-B under the same condition as that for fabricating PCN-S. The resulting light-yellow agglomerates were milled into powder in a mortar.

Physicochemical characterization

Transmission electron microscopy (TEM) analyses were conducted by a JEM-2100F electron microscope (JEOL, Japan) operating at 200 kV; moreover, the energy dispersive X-ray spectroscopy (EDX) profiles were recorded. Atomic force microscopy (AFM) analysis was performed on a NT-MDT Ntegra Solaris instrument. The Brunauer–Emmett–Teller (BET) surface area (S_{BET}) and pore volume (PV) of the samples were determined by N_2 adsorption using a Micromeritics ASAP 2020 N_2 adsorption apparatus (USA). XRD patterns were obtained on a powder X-ray diffractometer at 40 kV and 15 mA using Cu Kα radiation (Miniflex, Rigaku). Fourier transform infrared (FT-IR) spectra were acquired on a Nicolet 6700 (Thermoscientific) instrument. X-ray photoelectron spectroscopy (XPS) measurements were performed on an Axis Ultra (Kratos Analytical, UK) XPS spectrometer equipped with an Al Kα source (1486.6 eV). UV-Vis diffuse reflectance spectra were acquired for the dry-pressed disk samples by using a UV-Vis spectrophotometer (UV2600, Shimadzu, Japan) with $BaSO_4$ as the reflectance standard. Steady-state photoluminescence (PL) spectra were measured at room temperature on a RF-5301PC spectrofluorophotometer (Shimadzu, Japan) under the excitation of 350 nm. Time-resolved PL decay curves were recorded on a FLS920 fluorescence lifetime spectrophotometer (Edinburgh Instruments, UK) under the excitation of 365 nm and probed at 460 nm. Thermogravimetric analysis (TGA) was measured using a TGA/DSC 2 (Mettler-Toledo), over a range from room temperature to 800 °C with a ramp rate of 10 °C min^{-1} in an air flow of 40 mL min^{-1}.

Theoretical calculation

The spin-polarized density functional theory (DFT) calculations were carried out by using the Vienna ab initio simulation package (VASP).[53,54] The exchange-correlation interaction is described by generalized gradient approximation (GGA) with the Perdew-Burke-Ernzerhof (PBE) functional.[55] To better describe non-bonding interactions, Grimme's scheme Van der Waals correction is utilized. The energy cut-off is set to 500 eV. The Brillouin zone is sampled by a Monkhorst-Pack 6×6×1 K-point grid. The fully relaxed lattice constants are a = b = 6.95 Å for P-doped g-C_3N_4. HSE06 calculations[56,57] employing VASP are performed to get the exact band gaps of pure g-C_3N_4 and P-doped g-C_3N_4.

Photocatalytic H_2 production test

The experiments on photocatalytic H_2 evolution were accomplished in a 100 mL Pyrex flask (sealed with silicone rubber septa) at ambient temperature and atmospheric pressure. A Xe arc lamp (300 W) with a UV-cutoff filter (> 400 nm) was employed as a light source to trigger the photocatalytic reaction. In a typical photocatalytic experiment, 50 mg photocatalyst was suspended under constant stirring in a mixed solution of triethanolamine and water (TEOA, 20 vol%, as a sacrificial reagent). 1 wt% Pt was deposited onto the surface of photocatalysts by the *in-situ* photo-deposition approach using H_2PtCl_6 under Xe arc lamp (300 W) irradiation for 40 min. The suspension of the photocatalyst was bubbled with Argon gas for half an hour to remove air before

irradiation and guarantee the reactor in anaerobic conditions. 0.2 ml gas was sampled intermittently through the septum, and gas chromatograph (Clarus 480, PerkinElmer, USA, TCD with Ar as a carrier gas and 5 Å molecular sieve column) was employed to test the produced H_2. The apparent quantum efficiency (QE) was measured under the identical reaction condition. Four low-power LED (Shenzhen LAMPLIC Science Co. Ltd. China) at a wavelength of 420 nm, 460 nm, 500 nm, or 540 nm, which were put one cm away from the reactor in four different directions, were utilized as light sources to initiate the photocatalytic reaction. The apparent QE was calculated according to Equation (1):

$$QE[\%] = \frac{\text{number of reacted electrons}}{\text{number of incident photons}} \times 100$$
$$= \frac{\text{number of evolved } H_2 \text{ molecules}}{\text{number of incident photons}} \times 100 \quad (1)$$

Photoelectrochemical measurement

Mott-Schottky plots were recorded on an electrochemical analyzer (CHI 650D Instruments) with a standard three-electrode system using the synthesized samples coated on F-doped SnO_2-coated glass (FTO glass) as the working electrodes, a Pt wire as the counter electrode, and Ag/AgCl (saturated KCl) as a reference electrode. Electrochemical impedance spectra (EIS) measurements were also carried out on the above-mentioned three-electrode system. The EIS frequency ranged from 1 to 10^5 Hz with an alternating current amplitude of 10 mV. Transient photocurrents (TPC) were measured in the same three-electrode system. The light was produced by a 300 W Xe arc lamp. The working electrodes were synthesized as follows: 0.1 g photocatalyst was ground with 0.03 g polyethylene glycol (PEG; molecular weight: 20000) and 0.5 ml ethanol to make a slurry. The slurry was then coated onto a 2 cm*1.5 cm FTO glass electrode by the doctor blade method. The resulting electrodes were dried in an oven and heated at 350 °C for half an hour in a N_2 gas flow. All electrodes used had a similar film thickness of about 10-11 μm.

Results and discussion

Morphology and porous structure

PCN-S was synthesized by a combination of P doping and thermal exfoliation method as illustrated in Scheme 1. Firstly, ME and a new P precursor, AEP, were dissolved in water and tightly coupled via acid-base interaction and Van Der Waals' force.[58] After evaporation, the precipitated ME-AEP complex was subjected to thermal poly-condensation, thus yielding PCN-B. During this process, the ammonia gas released from the decomposition of AEP created many macropores on the layers of PCN-B, as confirmed by the SEM image (Fig. S2a in ESI†). Then, the thermal exfoliation gradually oxidized the hydrogen-bonded cohered strands of heptazine units in the layers of PCN-B, which reduced its thickness to several nano-

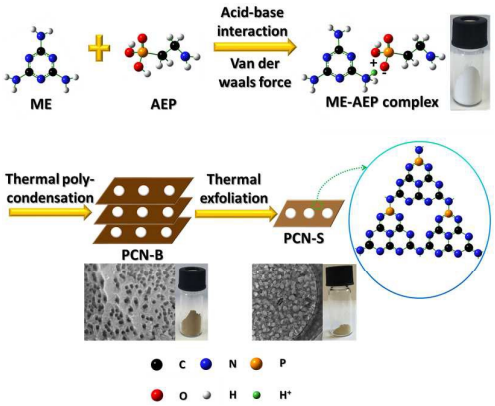

Scheme 1 Synthesis procedure of porous PCN-S.

meters and exposed these macropores, finally producing porous PCN-S. The morphology of PCN-S was analyzed by TEM and AFM. As shown in Fig. 1a, PCN-S features a novel macroporous nanosheets structure with lateral size of several micrometers. The high-magnification TEM image in Fig. 1a inset further displays that numerous macropores with sizes of 90-300 nm are homogeneously dispersed on the surface of PCN-S, associated with the uniform and intimate coupling between ME and AEP. In consistent with the TEM image, many macropores are also found on the surface of PCN-S in the AFM image (Fig. 1a inset). The thickness of PCN-S is determined to be *ca.* 5-8 nm as presented in Fig. 1a inset. Such an interesting porous nanosheets architecture of PCN-S can offer a large surface area for accommodating active sites, promote the ease diffusion of reactants and products molecules in the interconnected porous network, as well as enhance light harvesting. Besides, the ultrathin thickness of PCN-S also benefits the rapid transfer of photo-generated charge carriers from interior to the surface active sites, which are desirable for photocatalysis.[34-40] In comparison, CN-B shows a morphology of solid agglomerates in the size of several micrometers, while a wrinkled and non-porous nanosheets structure in micrometer size is observed for CN-S (see Fig. S3a and b in ESI†).

The unique porous nanosheets structure of PCN-S motivates us to further study its BET surface area and pore volume. Thus, the N_2 sorption isotherms of CN-B, CN-S, PCN-B and PCN-S were investigated. As shown in Fig. 1b, all the samples exhibit type IV isotherms, suggesting of well-defined mesopores.[60] As for PCN-S, it shows a H3-type hysteresis loop, indicating the presence of slit-like pores, derived from the overlapping and stacking of nanosheets. The isotherm of PCN-S presents high absorption at a high relative pressure (P/P_0), corresponding to the existence of large mesopores and macropores, in agreement with the TEM and AFM results. In addition, PCN-S exhibits a very broad pore size distribution in the 1-100 nm region, due to the random pores formation induced by the emission of ammonia gas (see the pores formation mechanism in Fig. S5 of ESI†). Furthermore, Table S1 shows quantitative details on BET surface areas and pore volumes of all the

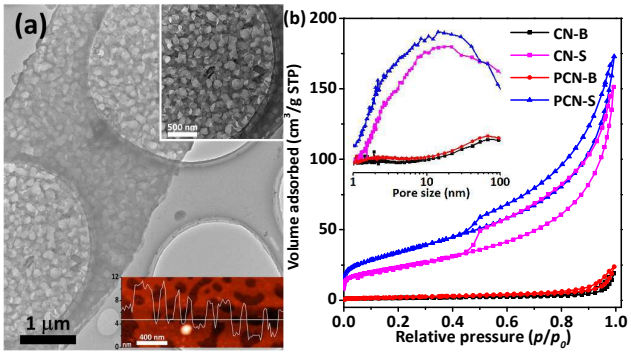

Fig. 1 (a) TEM image of PCN-S with inset showing the high-magnification TEM image, the AFM image and the corresponding height profile of PCN-S and (b) N_2 sorption isotherms of CN-B, CN-S, PCN-B and PCN-S with inset displaying the corresponding pore size distribution curves.

samples. PCN-S presents the largest BET surface area (122.6 $m^2 g^{-1}$) and pore volume (0.27 $cm^3 g^{-1}$), much higher than those of CN-B, CN-S or PCN-B. These data are in good consistence with the morphologies of these samples, which highlights the key role of this combinative method in creating such a distinctive texture of PCN-S.

Crystal structure and chemical states

To study the influence of P doping and thermal exfoliation on the crystal structure of PCN-S, all the samples were investigated by XRD. As displayed in Fig. S6a, CN-B exhibits two diffraction peaks of (100) and (002), which is consistent with bulk g-C_3N_4 (JCPDS 87-1526). Compared with CN-B, PCN-S shows similar features of the XRD patterns, indicating that the original crystal structure of g-C_3N_4 is largely retained after the P doping and thermal exfoliation. The FT-IR spectrum of PCN-S in Fig. S6b of ESI† provides further molecular structure information. The typical C-N heterocycle stretches in the 1200-1600 cm^{-1} region and the breathing mode of the heptazine units at 800 cm^{-1} are found in PCN-S,[15,19,20,38,39] as in unmodified CN-B. This suggests that the original g-C_3N_4 backbone remained almost unchanged, which is in coincidence with the above XRD results. Similar XRD and FT-IR results are also observed for CN-S and PCN-B (Fig. S6a and b, ESI†), thus proving that the 2D conjugated backbone structures of CN-S, PCN-B and PCN-S are well maintained, which is essential for π-delocalized electronic systems to generate and transport photo-excited electron-hole pairs for the subsequent redox reactions.[24]

Although no obvious change has occurred to the matrix network of PCN-S, the subtle alteration of crystal structure for PCN-S has been unveiled. The EDX spectrum in Fig. S7a (ESI†) confirms that PCN-S consists of C, N, and P elements, implying the successful doping of P in the PCN-S. XPS was further utilized to reveal the precise doping site of P in the PCN-S aromatic system. As presented in Fig. S7b (ESI†), a P 2p peak is observed at a binding energy of 133.1 eV for PCN-S, which corresponds to the P-N coordination, suggesting that P most probably replaces C in g-C_3N_4 to form P-N bonds.[26,61] Our calculation results further show that the more energy-

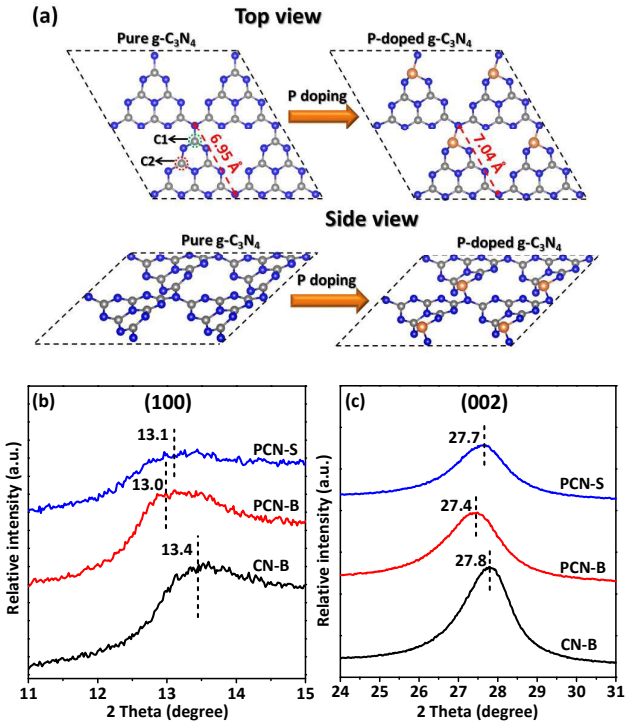

Fig. 2 (a) Top and side view of the optimized pure g-C_3N_4 and P-doped g-C_3N_4 configuration, color scheme: C, grey; N, blue; P, orange. Enlarged view of (100) peaks (b) and (002) peaks (c) for CN-B, PCN-B and PCN-S.

favorable C site for P doping is C1 instead of C2 in the heptazine unit (Fig. 2a). So we presume that all the doped P atoms replace C1 in the heptazine unit of PCN-S. Based on this assumption, the calculation results indicate that the in-planar distance of nitride pores is enlarged from 6.95 Å to 7.04 Å after P doping (Fig. 2a), due to the slight distortion of nitride pores by P incorporation.[62]

To confirm the calculation results, a further observation on the (100) and (002) peaks of XRD patterns is necessary. As shown in Fig. 2b, the low-angle diffraction peak (100) represents the in-plane structural packing motif or the heptazine units.[15,19,20,32,38,39] After P doping, PCN-B shows an obvious shift of (100) peak from 13.4° to 13.0° compared with CN-B, corresponding to the increase in the distance of in-planar nitride pores from 6.61 Å to 6.81 Å. This result is consistent with the above calculation result (Fig. 2a). Upon thermal exfoliation, PCN-S shows negligible change in (100) peak position but a greatly weakened peak intensity compared to PCN-B, implying that the in-planar layer size becomes much smaller due to the "etching effect" by thermal exfoliation.[39] Moreover, the high-angle diffraction peak (002) in Fig. 2c is a characteristic interlayer stacking reflection of conjugated aromatic systems.[15,20,31,35,38,39] In comparison to CN-B, an apparent shift of (002) peak from 27.8° to 27.4° is observed for PCN-B, suggesting that the interlayer distance is increased from 3.21 Å to 3.26 Å after P doping, attributed to the larger radius of doped P atom (100 pm) than that of replaced C atom (70 pm).[62] Thermal exfoliation of PCN-B leads to the shift of its

(002) peak from 27.4° to 27.7° for PCN-S, corresponding to the decrease of interlayer distance from 3.26 Å to 3.22 Å. The reason is that the heat treatment planarized the undulated single layers in PCN-B, thus resulting in the denser packing of layers in PCN-S.[39] In addition, the (002) peak intensity is obviously weakened for PCN-S, suggesting the layered PCN-B has been successfully exfoliated.[34-36] Therefore, the above results indicate that the combination of P doping and thermal exfoliation successfully leads to the doping of P in the aromatic system and the exfoliation of bulk g-C_3N_4 to g-C_3N_4 nanosheets for PCN-S.

Optical properties and electronic band structure

In view of solar energy utilization, it is of great importance to extend the light absorption spectrum for the photocatalysts, which can generate much more photo-excited electron-hole pairs for the following redox reactions.[10,14,16,17,21] Therefore, the optical property of PCN-S was studied by the UV-Vis diffuse reflectance spectra as shown in Fig. 3a. Based on the spectra, the band gap (E_g) energies of all the samples were acquired by the Kubelk-Munk method[63] (see Fig. S9a-d, ESI†) and summarized in Table S1. Compared with CN-B, PCN-S shows a blue shift of absorption edge, suggesting the increase of its band gap. In fact, although P doping can narrow the band gap of PCN-B to 2.68 eV compared with CN-B (2.78 eV), the subsequent thermal exfoliation enlarge the band gap of PCN-S to 2.91 eV, due to the strong QCE aroused by the ultrathin nanosheets structure.[35-40] Therefore, the light-harvesting capability (λ < 429 nm) originated from the band-gap absorption of PCN-S is seriously restricted in the visible-light region (400 nm < λ < 800 nm), which accounts for a large percentage (*ca.* 53%) in the solar spectrum.[4] Indeed, though the previous studies[34-40] show that the exfoliation of bulk g-C_3N_4 to form nanosheets can bring many benefits, a bottleneck of g-C_3N_4 nanosheets for achieving high-performance photocatalysis is their increased band gap, which severely limits its utilization of solar light. However, different from previous works,[34-40] PCN-S synthesized in this work shows a very strong tail absorption (Urbach tail) in the visible-light region. Usually, the Urbach tail is attributed to the electronic states located within the band gap (known as midgap states).[63,64]

To investigate the origin of these midgap states, the electronic structure of P-doped g-C_3N_4 was calculated by DFT studies. The results show that after P doping the intrinsic band gap of g-C_3N_4 is narrowed from 2.98 eV to 2.66 eV (Fig. 3b and c), and the empty midgap states arising from the hybridization of C 2s2p, N 2s2p and P 3s3p appear below the conduction band (CB) of g-C_3N_4 in Fig. S10b (ESI†). Hence, the empty midgap states can accommodate the electrons photo-excited from the valence band (VB) of P-doped g-C_3N_4, which greatly contributes to the absorption of photons with energies smaller than the band gap, thus resulting in the appearance of Urbach tail.[63,65,66] Therefore, it is not surprising that after P doping, Urbach tail absorption is observed for both PCN-B and PCN-S. In contrast, no Urbach tail is observed for the undoped CN-S and CN-B, confirming that it is P doping, instead of thermal exfoliation, induces the midgap states.

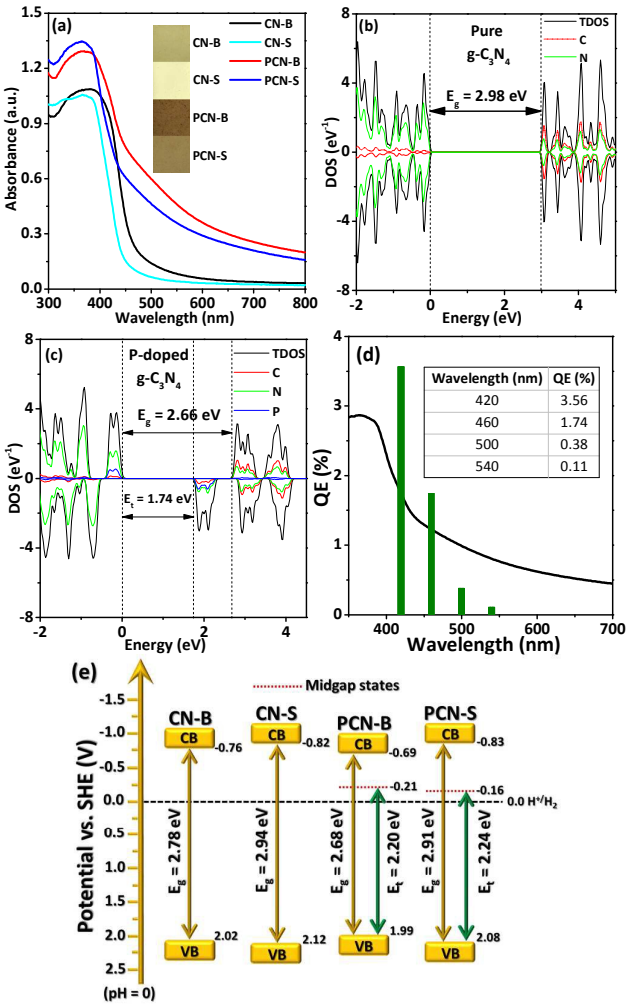

Fig. 3 (a) UV-Vis diffuse reflectance spectra of CN-B, CN-S, PCN-B, and PCN-S with inset showing the optical images of sample powders with different colours. Total density of states (TDOS) and partial density of states (PDOS) of (b) the pure g-C_3N_4 and (c) the P-doped g-C_3N_4. The Fermi level is set to the zero of energy. (d) QE of PCN-S at 420 nm, 460 nm, 500 nm or 540 nm. (e) Electronic band structures of CN-B, CN-S, PCN-B, and PCN-S.

To reveal whether the midgap states will promote the photocatalytic H_2 production, it is necessary to calculate their position in the band gap. Firstly, we acquired the CB and VB positions of PCN-S by investigating the electrochemical Mott-Schottky plot (Fig. S11d, ESI†). The flat band potential of PCN-S is found to be at -0.83 V *vs.* Standard Hydrogen Electrode (SHE). We used this value, combined with the band gap energy obtained in Fig. S9d (ESI†), to show the CB and VB positions of PCN-S in Fig. 3e. Then, the transition energy (E_t) from VB to the midgap states for PCN-S was calculated to be 2.24 eV by the Kubelk-Munk method in Fig. S9d (ESI†).[63] Finally, as shown in Fig. 3e, the exact position of midgap states for PCN-S was determined to be at -0.16 V *vs.* SHE, which is higher than the

H_2 evolving level ($2H^+ + 2e^- = H_2$, E^o = 0.0 V *vs.* SHE at pH = 0). This result suggests that the photo-generated electrons excited from VB to the midgap states are capable of reducing protons to evolve H_2 in thermodynamics. Thus, it is proposed that the presence of midgap states in PCN-S can allow the utilization of visible light with wavelength up to 557 nm for H_2 production. To confirm this conjecture, the QE of PCN-S for photocatalytic H_2 production at 420 nm, 460 nm, 500 nm or 540 nm were measured and summarized in the inset of Fig. 3d. Indeed, PCN-S shows QE even at wavelength longer than its band gap excitation (λ = 429 nm), *i.e.* 1.74% at 460 nm, 0.38% at 500 nm and 0.11% at 540 nm. Similarly, PCN-B also exhibits QE at wavelength above its band gap absorption (λ = 466 nm) as displayed in Fig. S12c (ESI†). In comparison, without the existence of midgap states, neither CN-B nor CN-S shows any QE at 460 nm, 500 nm or 540 nm (see Fig. S12a and b, ESI†). Hence, the above results firmly support that the midgap states induced by P doping play a key role in enhancing the visible-light absorption of PCN-S for photocatalytic H_2 production. Besides, unlike the previously reported g-C_3N_4 nanosheets,[34-40] the novel macroporous structure of PCN-S can further improve light harvesting by multiple inner reflections of the incident light,[51,52] thus leading to a synergistic enhancement in visible-light absorption.

Charge-carrier separation and transport

The combination of P doping and thermal exfoliation routes leads to the P-doped aromatic system and porous nanosheets architecture of PCN-S, thus endowing it with outstanding light-harvesting ability, short charge-to-surface diffusion length and large surface area. However, whether this combinative synthesis method can achieve the desired synergistic effect on the photocatalytic activity, a key question needs to be answered: can the electron-hole pairs photo-excited in PCN-S be efficiently separated and transferred to surface for the desired redox reactions other than trapped and recombined with each other? To answer this question, the combined techniques of steady-state and time-resolved PL spectroscopy, as well as EIS were employed to investigate the charge separation and transfer behaviours in PCN-S.

Fig. S13 shows the steady-state PL spectra of CN-B, CN-S, PCN-B and PCN-S at 350 nm excitation light. Compared with CN-B, PCN-B shows a much lower PL peak intensity, suggesting a suppressed photo-generated charge recombination, due to the increased charge diffusion rate in the P-doped heptazine aromatic system. This is because after forming three covalent bonds with the adjacent N atoms, the remaining lone electron pairs of incorporated P is delocalized to the P-doped aromatic system, thus increasing the charge density and mobility of PCN-B.[61] On the other hand, the low charge recombination observed in PCN-B also confirms that the midgap states induced by P doping don't act as a recombination center trapping the electron-hole pairs. Instead, they serve as the separation centers to capture the photo-generated electrons, and inhibit the charge recombination.[67,68] As for CN-S, it also shows a lower PL peak intensity than that of CN-B, implying that its ultrathin thickness facilitates the efficient separation and transfer of charge carriers. Besides, the enlarged bandgap due to QCE also promotes the separation of charge carriers.[39] Among all the samples, the smallest PL peak intensity is found for PCN-S, suggesting its lowest charge recombination rate. This is very important because it confirms that the subsequent thermal exfoliation after P doping does not impair the electronic structure of the P-doped aromatic system or create abundant trap-site defects in PCN-S, which can seriously impede the charge separation and transfer.[15] In fact, the combinative synthesis method successfully merges the above merits created by P doping and thermal exfoliation in PCN-S, thus exerting a synergistic effect on impeding the charge recombination.

It is well known that the charge carriers lifetime plays a pivotal role in determining the probability of their involvement in the photocatalytic reactions before their recombination.[39,50,69,70] That is, a longer charge carrier lifetime usually represents a higher possibility of their participation in the photocatalytic reactions, thus implying a better photocatalytic activity.[39] Hence, to gain a quantitative knowledge of the photo-generated charge carrier lifetime in all the samples, the time-resolved PL spectra are investigated and displayed in Fig. 4a. Firstly, the PL lifetimes of all the samples are calculated by fitting the time-resolved PL decay curves with the following exponential fitting Equation (2)[50]:

$$\text{Fit} = A + B_1\exp\left\{-\frac{t}{\tau_1}\right\} + B_2\exp\left\{-\frac{t}{\tau_2}\right\} \quad (2)$$

where A, B_1, B_2 are constants and obtained after fitting every decay curve. This equation generates a fast (τ_1) and slow (τ_2) decay component, respectively.[70] Then, on basis of the above fitting data, the intensity-average lifetime (τ) is calculated and presented to make an overall comparison of the PL lifetimes of all the samples by the following Equation (3)[69]:

$$\tau = \frac{B_1\tau_1^2 + B_2\tau_2^2}{B_1\tau_1 + B_2\tau_2} \quad (3)$$

Finally, all the fitting PL decay data are summarized and listed in Table S2 (ESI†). Compared with CN-B, CN-S, PCN-B and PCN-S show increased short (τ_1), long (τ_2) and intensity-average (τ) PL lifetimes, suggesting that the P doping and/or thermal exfoliation can effectively elongate the lifetime of charge carriers. In particular, PCN-S shows the longest lifetime (τ_1 = 3.927 ns) for a majority of charge carriers (67.6%), while PCN-B presents a shorter lifetime (τ_1 = 3.460 ns) for 64.1% charge carriers, followed by CN-S (τ_1 = 3.325 ns) for 65.1% charge carriers. In an obvious contrast, CN-B exhibits the shortest lifetime (2.885 ns) for a large percentage (67.15%) of charge carriers. Therefore, the above fitting data solidly corroborate that the lifetimes of charge carriers in PCN-S are synergistically lengthened by the combinative synthesis method.

The above two techniques highlight the high separation and transfer efficiency of photo-generated electron-hole pairs in

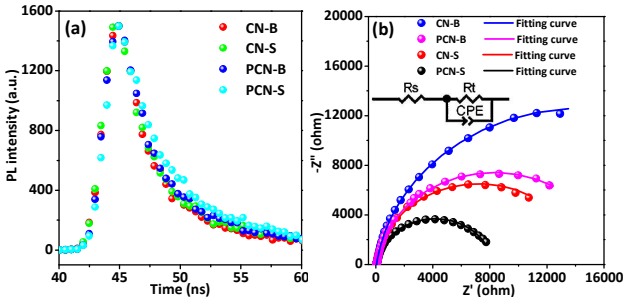

Fig. 4 (a) Time-resolved PL decay spectra of CN-B, CN-S, PCN-B and PCN-S at λ_{ex} = 368 nm. (b) EIS Nyquist plots of CN-B, CN-S, PCN-B and PCN-S electrodes in 0.2 M Na_2SO_4 aqueous solution.

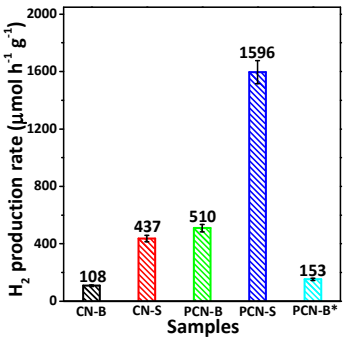

Fig. 5 Comparison of the photocatalytic activity of CN-B, CN-S, PCN-B, PCN-S and PCN-B* for the H_2 production using 20 v% triethanolamine (TEOA) aqueous solution as a sacrificial reagent under visible-light irradiation (⩾ 400 nm, 300 W Xe lamp).

PCN-S upon light irradiation. However, the charge transport process occurring in PCN-S under dark condition, which directly reflects its capacity to shuttle and convey charge carriers to the targeted reactive sites[40,71] is still unknown. Thus, to obtain a deep insight into the charge transport behaviour of PCN-S in the absence of light excitation, EIS measurements were carried out under dark condition. Fig. 4b displays the EIS Nyquist plots of all the samples. In fact, the EIS Nyquist plots can be well simulated to the equivalent electrical circuit as shown in Fig. 4b inset, in which R_s and R_t are the electrolyte solution resistance and the interfacial charge-transfer resistance/electrolyte, respectively.[71] Based on the above model, the fitting data of all the samples are summarized in Table S3 (ESI†). Among all the samples, PCN-S shows the smallest diameter and R_t value, suggesting its lowest resistance for interfacial charge transfer from electrode to electrolyte molecules. Therefore, combined with the above steady-state and time-resolved PL spectroscopy, it is deemed that PCN-S possesses the strongest capability to not only separate photo-generated electron-hole pairs, but also transfer them to the reactant molecules adsorbed on the surface active sites, implying its outstanding competence as a high-performance photocatalyst.

Photocatalytic performance and mechanism

Fig. 5 shows a comparison of photocatalytic H_2-production activities of CN-B, CN-S, PCN-B, PCN-S and PCN-B*. CN-B only exhibits a very low photocatalytic H_2-production rate of 108 μmol h^{-1} g^{-1}, arising from its limited visible-light absorption, low surface area and poor charge transport capability. The thermal exfoliation of CN-B to ultrathin CN-S leads to an obvious increase in the photocatalytic H_2-production activity from 108 μmol h^{-1} g^{-1} to 437 μmol h^{-1} g^{-1} due to the enlarged surface area, shortened electron-hole transfer distance and increased redox capabilities of electrons and holes. Moreover, PCN-B acquired by P doping also exhibits an apparent enhancement in photocatalytic H_2-production rate to 510 μmol h^{-1} g^{-1}, mainly due to the significant increase of visible-light harvesting and charge diffusion rate. In fact, this enhancement factor is the highest among all P-doped g-C_3N_4 applied in photocatalytic H_2 production.[20,26] This is believed to result from the strong and uniform coupling between ME and AEP via acid-base interaction and Van Der Waals' force (Scheme 1).[58] Indeed, PCN-B* synthesized by using the inorganic P precursor, $(NH_4)_2HPO_4$, shows a much lower photocatalytic H_2-production activity (153 μmol h^{-1} g^{-1}) than that of PCN-B. The major reason is that the organic characteristic of AEP leads to better interaction with ME, and its higher decomposition temperature (above 250 °C, see Fig. S14 in ESI†) than that of $(NH_4)_2HPO_4$ promotes more substantial and homogeneous doping of P in the g-C_3N_4 backbone (as confirmed by elemental mapping images in Fig. S2a-d and Fig. S15a-d). This is because AEP is more thermally stable when poly-condensation of ME begins.[58] Besides, the higher graphitic degree in PCN-B than that in PCN-B*, as suggested by the larger content of graphic carbon for PCN-B (Fig. S16, ESI†), also contributes to its enhanced conductivity and better photocatalytic activity. Thus, this result underscores the great importance of selecting the appropriate doping precursor to maximize the enhancement of photocatalytic activity. Surprisingly, PCN-S shows the highest photocatalytic H_2-production activity of 1596 μmol h^{-1} g^{-1}, which is 14.8 times higher than that of CN-B (108 μmol h^{-1} g^{-1}), and even much higher than the sum by CN-S and PCN-B. Such an impressive photocatalytic activity and high QE (3.56 % at 420 nm) for PCN-S represents one of the most highly-active metal-free g-C_3N_4 nanosheets photocatalysts.[34-40] Notably, the combinative synthesis method in this work is facile, environmental-benign and easy for scale up, without using any templates or organic/acid chemicals for acquiring porous or nanosheets structures.

On basis of the above results, the photocatalytic H_2-production mechanism of PCN-S can be proposed. It is widely accepted that four consecutive steps are included in various photocatalytic reactions as follows: i) light absorption; ii) photo-excitation to produce electron-hole pairs; iii) electron-hole pairs separation and migration to photocatalyst surface; iv) surface adsorption and redox reaction.[2,3,7] Since the above four steps are intimately associated with the intrinsic characteristics of a photocatalyst system, such as electronic, crystal, surface and textural structures, an integrated engineering of the above properties would enable a synergetic tuning and optimization of the four consecutive steps, thus

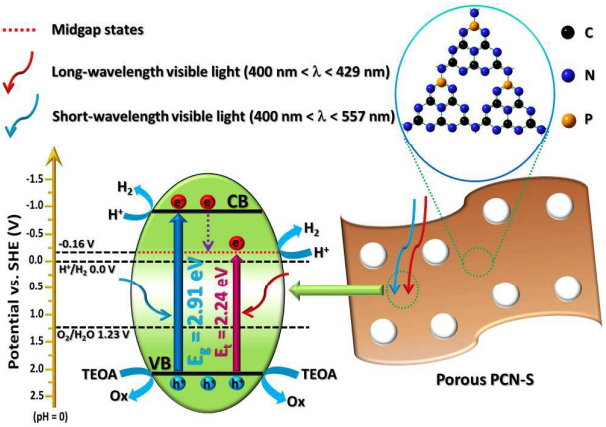

Fig. 6 Photocatalytic H_2-production mechanism of porous PCN-S.

achieving a maximum improvement of the photocatalytic performance.[72] PCN-S prepared in this work is just an example. Firstly, both the electronic structure and texture of PCN-S has been modified to harvest more visible light. As displayed in Fig. 6, although PCN-S can only absorb visible light with wavelength below 429 nm (400 nm < λ < 429 nm) due to its large band gap (2.91 eV), the midgap states induced by P doping can extend the visible-light absorption region up to 557 nm (400 nm < λ < 557 nm). Thus, PCN-S can harvest both short- and long-wavelength visible light to photo-excite the electrons in the VB to the CB and the midgap states, respectively, while leaving the photo-generated holes in the VB. On the other hand, the macroporous structure of PCN-S can increase the optical path by multiple scattering effect, thus enhancing light harvesting.[51,52] Secondly, the electronic and textural structures are simultaneously tuned to optimize the separation and transfer of photo-generated electron-hole pairs. In detail, not only the charge mobility is greatly improved in P-doped aromatic system, but also the diffusion path from internal towards the surface is significantly contracted. As a result, electron-hole pairs photo-excited in the interior of PCN-S can either rapidly transfer to the surface along the interlayer direction, due to the ultrathin thickness of PCN-S, or migrate to the walls of many macropores in PCN-S; whilst electron-hole pairs photo-excited on the surface of PCN-S can promptly move to the reactive sites along the in-plane direction. Besides, the midgap states can also serve as separation centers to temporarily trap photo-generated electrons from the CB and thus promote the separation of electron-hole pairs (Fig. 6). Finally, both the surface and textural structures are tailored to supply more surface area for accommodating massive absorption and catalytic-active centers, as well as facilitate the rapid transfer of reactants and products through the porous network. Actually, the combinative method synergistically enlarges the surface area of PCN-S, which not only includes the horizontal surface of nanosheets, but also the walls of numerous macropores. Thus, a large number of protons/TEOA molecules in the reaction solution can easily get access to the abundant adsorption centers on the surface of PCN-S, after which interfacial electrons/holes transfer from surface to adsorbed protons/TEOA molecules occur. At last, protons/TEOA molecules undergo surface redox reactions in the catalytic centers, producing H_2/oxidative products (Ox). Meanwhile, the macroprous structure of PCN-S benefits the whole mass-transfer process during the adsorption and catalytic reaction. Therefore, the combinative method simultaneously tailors the electronic, crystal, surface and textural structures to optimize the four consecutive steps in photocatalytic H_2 production. As a result, a strong synergetic enhancement in the photocatalytic activity is achieved.

To provide additional evidence for the above suggested photocatalytic mechanism, the TPC measurement was performed. As can be see from Fig. S17a (ESI†), the TPC densities of CN-B, CN-S, PCN-B and PCN-S show the same trend as their photocatalytic activities (Fig. 5), thus further supporting the above photocatalytic mechanism.

Moreover, the stability of PCN-S was also tested by operating the photocatalytic experiments under the same reaction conditions for four cycles (Fig. S17b, ESI†). No noticeable deterioration of activity is observed, indicating the robustness of PCN-S.

Conclusions

In summary, a novel method combining P doping and thermal exfoliation was developed to prepare a new porous P-doped g-C_3N_4 nanosheets photocatalyst. The new photocatalyst exhibits enhanced visible-light absorption (up to 557 nm), enlarged surface area (122.6 m^2 g^{-1}), shortened charge-to-surface migration length (5-8 nm) and improved charge mobility, due to its P-doped aromatic system and macroporous nanosheets architecture. Thus, a very high visible-light photocatalytic H_2-production activity of 1596 μmol h^{-1} g^{-1} and an apparent quantum efficiency of 3.56% at 420 nm were achieved by this new photocatalyst. Notably, the theoretical and experimental studies for the first time reveal that the empty midgap states (-0.16 V *vs.* SHE) induced by P doping significantly contribute to the visible-light photocatalytic H_2 production. This work highlights that an easy and green route can be utilized to prepare a high-efficiency porous g-C_3N_4 nanosheets photocatalyst, which opens a new window for the tailor design and fabrication of highly-active metal-free photocatalyst for solar-light-driven H_2 production.

Acknowledgements

This work was supported financially by the Australian Research Council (ARC) through the Discovery Project program (DP140104062 and DP130104459).

References

1 A. Fujishima and K. Honda, *Nature*, 1972, **238**, 37.
2 J. Ran, J. Zhang, J. Yu, M. Jaroniec and S. Z. Qiao, *Chem. Soc. Rev.*, 2014, **43**, 7787.

3 S. Chen, S. Shen, G. Liu, Y. Qi, F. Zhang and C. Li, *Angew. Chem. Int. Ed.*, 2015, **54**, 3047.
4 J. Ran, J. Yu and M. Jaroniec, *Green Chem.*, 2011, **13**, 2708.
5 K. Chang, Z. Mei, T. Wang, Q. Kang, S. Ouyang and J. Ye, *ACS Nano*, 2014, **8**, 7078.
6 H. Li, Y. Zhou, W. Tu, J. Ye and Z. Zou, *Adv. Funct. Mater.*, 2015, **25**, 998.
7 A. Kudo and Y. Miseki, *Chem. Soc. Rev.*, 2009, **38**, 253.
8 K. Ueda, T. Minegishi, J. Clune, M. Nakabayashi, T. Hisatomi, H. Nishiyama, M. Katayama, N. Shibata, J. Kubota, T. Yamada and K. Domen, *J. Am. Chem. Soc.*, 2015, **137**, 2227.
9 X. Wang, K. Maeda, A. Thomas, K. Takanabe, G. Xin, J. M. Carlsson, K. Domen and M. Antonietti, *Nat. Mater.*, 2009, **8**, 76.
10 J. S. Zhang, J. H. Sun, K. Maeda, K. Domen, P. Liu, M. Antonietti, X. Z. Fu and X. C. Wang, *Energy Environ. Sci.*, 2011, **4**, 675.
11 J. Liu, Y. Liu, N. Liu, Y. Han, X. Zhang, H. Huang, Y. Lifshitz, S. Lee, J. Zhong and Z. Kang, *science*, 2015, **347**, 970.
12 S. Cao, J. Low, J. Yu and M. Jaroniec, *Adv. Mater.*, 2015, **27**, 2150.
13 S. Cao and J. Yu, *J. Phys. Chem. Lett.*, 2014, **5**, 2101.
14 S. C. Yan, Z. S. Li and Z. G. Zou, *Langmuir*, 2010, **26**, 3894.
15 Z. Lin and X. Wang, *Angew. Chem. Int. Ed.,* 2013, **52**, 1735.
16 G. Dong, K. Zhao and L. Zhang, *Chem. Commun.*, 2012, **48**, 6178.
17 J. Li, B. Shen, Z. Hong, B. Lin, B. Gao and Y. Chen, *Chem. Commun.*, 2012, **48**, 12017.
18 Y. Wang, Y. Di, M. Antonietti, H. Li, X. Chen and X. Wang, *Chem. Mater.*, 2010, **22**, 5119.
19 L. Zhang, X. Chen, J. Guan, Y. Jiang, T. Hou and X. Mu, *Mater. Res. Bull.*, 2013, **48**, 3485.
20 S. Hu, L. Ma, J. You, F. Li, Z. Fan, G. Lu, D. Liu and J. Gui, *Appl. Surf. Sci.*, 2014, **311**, 164.
21 G. Liu, P. Niu, C. Sun, S. C. Smith, Z. Chen, G. Q. M. Lu and H.-M. Cheng, *J. Am. Chem. Soc.*, 2010, **132**, 11642.
22 J. Hong, X. Xia, Y. Wang and R. Xu, *J. Mater. Chem.*, 2012, **22**, 15006.
23 L. Ge, C. Han, X. Xiao, L. Guo and Y. Li, *Mater. Res. Bull.*, 2013, **48**, 3919.
24 G. Zhang, M. Zhang, X. Ye, X. Qiu, S. Lin and X. Wang, *Adv. Mater.*, 2014, **26**, 805.
25 S. Hu, L. Ma, J. You, F. Li, Z. Fan, F. Wang, D. Liu and J. Gui, *RSC Adv.*, 2014, **4**, 21657.
26 Y. Zhou, L. Zhang, J. Liu, X. Fan, B. Wang, M. Wang, W. Ren, J. Wang, M. Li and J. Shi, *J. Mater. Chem. A*, 2015, **3**, 3862.
27 X. Wang, X. Chen, A. Thomas, X. Fu and M. Antonietti, *Adv. Mater.*, 2009, **21**, 1609.
28 Z. Ding, X. Chen, M. Antonietti and X. Wang, *ChemSusChem*, 2011, **4**, 274.
29 J. Tian, Q. Liu, A. M. Asiri, A. H. Qusti, A. O. Al-Youbi and X. Sun, *Nanoscale*, 2013, **5**, 11604.
30 S. Tonda, S. Kumar, S. Kandula and V. Shanker, *J. Mater. Chem. A*, 2014, **2**, 6772.
31 J. Zhang, X. Chen, K. Takanabe, K. Maeda, K. Domen, J. D. Epping, X. Fu, M. Antonietti and X. Wang, *Angew. Chem. Int. Ed.*, 2010, **49**, 441.
32 J. Zhang, G. Zhang, X. Chen, S. Lin, L. Mohlmann, G. Dolega, G. Lipner, M. Antonietti, S. Blechert and X. Wang, *Angew. Chem. Int. Ed.*, 2012, **51**, 3183.
33 S. Chu, Y. Wang, Y. Guo, J. Feng, C. Wang, W. Luo, X. Fan and Z. Zou, *ACS Catal.*, 2013, **3**, 912.
34 S. Yang, Y. Gong, J. Zhang, L. Zhan, L. Ma, Z. Fang, R. Vajtai, X. Wang and P. M. Ajayan, *Adv. Mater.*, 2013, **25**, 2452.
35 X. She, H. Xu, Y. Xu, J. Yan, J. Xia, L. Xu, Y. Song, Y. Jiang, Q. Zhang and H. Li, *J. Mater. Chem. A*, 2014, **2**, 2563.
36 H. Zhao, H. Yu, X. Quan, S. Chen, H. Zhao and H. Wang, *RSC Adv.*, 2014, **4**, 624.
37 Qi. Lin, L. Li, S. Liang, M. Liu, J. Bi and L. Wu, *Appl. Catal., B*, 2015, **163**, 135.
38 J. Xu, L. Zhang, R. Shi and Y. Zhu, *J. Mater. Chem. A*, 2013, **1**, 14766.
39 P. Niu, L. Zhang, G. Liu and H.-M. Cheng, *Adv. Funct. Mater.*, 2012, **22**, 4763.
40 H. Xu, J. Yan, X. She, L. Xu, J. Xia, Y. Xu, Y. Song, L. Huang and H. Li, *Nanoscale*, 2014, **6**, 1406.
41 H. Yan, *Chem. Commun.*, 2012, **48**, 3430.
42 J. Sun, J. Zhang, M. Zhang, M. Antonietti, X. Fu and X. Wang, *Nat. Commun.*, 2012, **3**, 1139.
43 Y. Zheng, L. Lin, X. Ye, F. Guo and X. Wang, *Angew. Chem. Int. Ed.,* 2014, **53**, 11926.
44 Y.-S. Jun, J. Park, S. U. Lee, A. Thomas, W. H. Hong and G. D. Stucky, *Angew. Chem. Int. Ed.*, 2013, **52**, 11083.
45 Y.-S. Jun, E. Z. Lee, X. Wang, W. H. Hong, G. D. Stucky and A. Thomas, *Adv. Funct. Mater.*, 2013, **23**, 3661.
46 M. Shalom, S. Inal, C. Fettkenhauer, D. Neher and M. Antonietti, *J. Am. Chem. Soc.*, 2013, **135**, 7118.
47 F. Dong, Z. Zhao, T. Xiong, Z. Ni, W. Zhang, Y. Sun and W. K. Ho, *ACS Appl. Mater. Interfaces*, 2013, **5**, 11392.
48 Y. Yang, W. Guo, Y. Guo, Y. Zhao, X. Yuan and Y. Guo, *J. Hazard. Mater.*, 2014, **271**, 150.
49 S. Min and G. Lu, *J. Phys. Chem. C*, 2012, **116**, 19644.
50 X. Zhang, L. Yu, C. Zhuang, T. Peng, R. Li and X. Li, *ACS Catal.*, 2014, **4**, 162.
51 X. Zhang, Y. Liu, S.-T. Lee, S. Yang and Z. Kang, *Energy Environ. Sci.*, 2014, **7**, 1409.
52 M.-Y. Tsang, N. E. Pridmore, L. J. Gillie, Y.-H. Chou, R. Brydson and R. E. Douthwaite, *Adv. Mater.*, 2012, **24**, 3406.
53 G. Kresse and J. Furthmüller, *Phys. Rev. B*, 1996, **54**, 11169.
54 G. Kresse and J. Furthmüller, *Comp. Mater. Sci.*, 1996, **6**, 15.
55 J. Perdew, K. Burke and M. Ernzerhof, *Phys. Rev. Lett.*, 1996, **77**, 3865.
56 J. Paier, M. Marsman, K. Hummer, G. Kresse, I. C. Gerber and J. G. Ángyán, *J. Chem. Phys.*, 2006, **124**, 154709.
57 J. Paier, M. Marsman, K. Hummer, G. Kresse, I. C. Gerber and J. G. Ángyán, *J. Chem. Phys.*, 2006, **125**, 249901.
58 T. Y. Ma, J. Ran, S. Dai, M. Jaroniec and S. Z. Qiao, *Angew. Chem. Int. Ed.*, 2015, **54**, 4646.
59 M. Zhang, J. Xu, R. Zong and Y. Zhu, *Appl. Catal., B*, 2014, **147**, 229.
60 J. Yu and J. Ran, *Energy Environ. Sci.*, 2011, **4**, 1364.
61 Y. Zhang, T. Mori, J. Ye and M. Antonietti, *J. Am. Chem. Soc.*, 2010, **132**, 6294.
62 J. Chen, Z. Hong, Y. Chen, B. Lin and B. Gao, *Mater. Lett.*, 2015, **145**, 129.
63 H. Yaghoubi, Z. Li, Y. Chen, H. T. Ngo, V. R. Bhethanabotla, B. Joseph, S. Ma, R. Schlaf and A. Takshi, *ACS Catal.*, 2015, **5**, 327.
64 J. Zhang, S. Liu, J. Yu and M. Jaroniec, *J. Mater. Chem.*, 2011, **21**, 14655.
65 S. John, C. Soukoulis, M. H. Cohen and E. N. Economou, *Phys. Rev. Lett.*, 1986, **57**, 1777.
66 R. Beranek and H. Kisch, *Photochem. Photobiol. Sci.*, 2008, **7**, 40.
67 N. Seriani, C. Pinilla and Y. Crespo, *J. Phys. Chem. C* 2015, **119**, 6696.
68 G. Wang, B. Huang, Z. Li, Z. Lou, Z. Wang, Y. Dai and M. Whangbo, *Sci. Rep.*, 2015, **5**, 8544.
69 Z. Zhang, J. Huang, M. Zhang, Q. Yuan and B. Dong, *Appl. Catal., B*, 2015, **163**, 298.
70 Y. Chen, T. Liu and Y. Hsu, *ACS Appl. Mater. Interfaces*, 2015, **7**, 1616.
71 J. Ran, J. Zhang, J. Yu and S. Z. Qiao, *ChemSusChem*, 2014, **7**, 3426.
72 S. Liu, J. Xia and J. Yu, *ACS Appl. Mater. Interfaces,* 2015, **7**, 8166.

The global energy crisis and environmental problems drive the aggressive search for a clean and renewable energy source to replace fossil fuels. The production of clean and carbon-free hydrogen energy from inexhaustible solar energy through photocatalytic water splitting is a 'dream technology' to address the worldwide energy shortage, environmental contamination and greenhouse effect. The core challenge of this advanced technology lies in the development of low-cost and environmental-benign photocatalysts with sufficiently high activity and stability to produce hydrogen at a cost comparable to the conventional fossil fuels. Herein, a simple, environmental-friendly and scalable strategy is firstly reported to fabricate a porous P-doped graphitic carbon nitride (g-C_3N_4) nanosheets photocatalyst. This photocatalyst exhibits both outstanding activity and stability for visible-light photocatalytic H_2 production, due to the strong synergistic effect by the P-doped conjugated system and novel macroporous nanosheets structure. This work demonstrates a new green and scalable technique to synthesize high-performance metal-free g-C_3N_4 photocatalyst. The novel g-C_3N_4 nanomaterials are also expected to be promising for other solar energy conversion applications, such as photovoltaic and photo-electrochemical water splitting devices.

,